J. Mech. Phys. Solids 190 (2024) 105741

Contents lists available at ScienceDirect

Journal of the Mechanics and Physics of Solids

journal homepage: www.elsevier.com/locate/jmps

Mechanics and thermal analyses of microfluidic nerve-cooler system

Dongjun Bai [a,c,1], Zichen Zhao [a,b,1], Raudel Avila [d], Danli Xia [a,b], Yonggang Huang [e,f,g,h], John A. Rogers [e,f,i,j], Zhaoqian Xie [a,b,c,*]

[a] State Key Laboratory of Structural Analysis, Optimization and CAE Software for Industrial Equipment, Dalian University of Technology, Dalian 116024, PR China
[b] Department of Engineering Mechanics, Dalian University of Technology, Dalian 116024, PR China
[c] DUT-BSU Joint Institute, Dalian University of Technology, Dalian 116024, PR China
[d] Department of Mechanical Engineering, Rice University, Houston, TX 77005, United States
[e] Department of Materials Science and Engineering, Northwestern University, Evanston, IL 60208, United States
[f] Querrey Simpson Institute for Bioelectronics, Northwestern University, Evanston, IL 60208, United States
[g] Department of Mechanical Engineering, Northwestern University, Evanston, IL 60208, United States
[h] Departments of Civil and Environmental Engineering, Northwestern University, Evanston, IL 60208, United States
[i] Department of Biomedical Engineering, Northwestern University, Evanston, IL, USA
[j] Department of Neurological Surgery, Feinberg School of Medicine, Northwestern University, Chicago, IL, USA

ARTICLE INFO

Keywords:
Fluid flow
Tissue strain
Phase change
Vaporization
Localized cooling

ABSTRACT

Recent advances in microelectronics and biomedical technology has led to capabilities for integrating programmable cooling mechanisms into bioelectronic devices for pain management and other important applications in human health. However, achieving localized and precise targeted cooling remains a challenge due to the influence of tissue mechanics during device placement/operation, viscous effects in the flow of coolants, and critical physical parameters that locally affect tissue temperature and mechanical responses. Recent studies demonstrate that bioelectronic devices can be equipped with microfluidic structures designed to support phase-change cooling mechanisms, with cooling power adjustable by control of fluid flow rates. When operated in closed-loop feedback schemes based on measurements of temperature at the tissue interface, these platforms can achieve precise temperature control of regions of peripheral nerves involved in pain signaling. Establishing a theoretical model to understand the effects of these devices on the underlying soft and deformable tissues, along with microfluidic deformations that can alter the heat transfer cooling process in viscous flow, is critical for optimized design and operation. To address this, a theoretical model is developed to describe the influence of remote strain in the tissue and to quantify the spatial temperature distribution of tissue cooled by fluid phase change in deformable microfluidic channels. A scaling law is derived to quantify the steady-state temperature distribution in the tissue under physiologically relevant mechanical loads, fluid viscosity, flow rates, and thermal conductivities, enabling the prediction of liquid and gas flux based on expected temperature changes and saturated vapor pressure in the deformed tissue and microchannel. These findings reveal that within a reasonable physiological range, the influence of fluid viscosity on temperature changes can be neglected, and the ratio of fluid to tissue thermal

* Corresponding author.
E-mail address: zxie@dlut.edu.cn (Z. Xie).
[1] These authors contributed equally to this work.

https://doi.org/10.1016/j.jmps.2024.105741
Received 1 April 2024; Received in revised form 22 May 2024; Accepted 9 June 2024
Available online 20 June 2024

conductivity minimally impacts the temperature change at relatively high flow rates. Additionally, the model suggests a limit to tissue cooling for a given fluid, which may not necessarily increase with higher fluid volumes.

T	Temperature in the tissue (K)
T_0	Environment temperature (K)
ΔT	Temperature difference T-T_0 (K)
ΔH	Enthalpy change due to liquid evaporation (J/mol)
p_0	Initial pressure in the microfluidic channel (Pa)
p	Pressure in the microfluidic channel after tissue deformation (Pa)
Δp	Pressure change p-p_0 in the microfluidic channel (Pa)
Vol_0	Initial volume of the microfluidic channel (m^3)
Vol	Volume of the microfluidic channel after tissue deformation (m^3)
ε	Applied strain in the tissue
E	Elastic modulus of the tissue (Pa)
υ	Poisson's ratio of the tissue
μ_f	Viscosity of the gas (kg/m·s)
P	Saturated vapor pressure (Pa)
P_0	Standard atmospheric pressure (Pa)
ξ	Liquid-to-gas molar ratio
X	Gas passing through per unit time before liquid evaporation (mol/s)
β	Volume fraction of the mixed gases after liquid evaporation
γ	Mass fraction of the mixed gases after liquid evaporation
v	Average flow rate of the mixed gases after liquid evaporation (m/s)
d	Diameter of the microfluidic channel (m)
d'	Diameter of the deformed microfluidic channel (m)
Q	Heat absorption per unit time due to liquid evaporation (W)
ρ_f	Density of the mixed gases after liquid evaporation (kg/m^3)
c_f	Specific heat capacity of the mixed gases after liquid evaporation [J/(kg ·K)]
λ_f	Thermal conductivity of the mixed gases after liquid evaporation [W/(m ·K)]
λ_t	Thermal conductivity of the tissue [W/(m·K)]
V_m	University constant 0.00224 m^3/mol of gas molar volume (m^3/mol)
M_A, M_B	Molar mass of gas A and gas B (kg/mol)
c_A, c_B	Specific heat capacity of gas A and gas B [J/(kg ·K)]
ρ_A, ρ_B	Density of gas A and gas B (kg/m^3)
λ_A, λ_B	Thermal conductivity of gas A and gas B [W/(m·K)]
ΔT^*	Average temperature over the cross-section of reaction ($z = 0$) in the microfluidic channel (K)

1. Introduction

Thermal management, the mechanism for regulating temperature or heat transfer in designated areas of interest through specialized materials, interfaces, and design or thermal techniques, finds extensive technological application across various engineering and scientific fields (Do et al., 2022; Ghasemi Zavaragh et al., 2017; Habibi Khalaj and Halgamuge, 2017; Kong et al., 2023; Zhai et al., 2022). Cooling and regulated temperature reduction is a critical aspect of thermal management and holds significant importance for ensuring safety operation of engineering systems (Rao et al., 2022; Weng et al., 2022; Zhang et al., 2024), enhancing micro-electro-mechanical systems (MEMS) performance (Li et al., 2010), advancing medical diagnosis and treatments (Do et al., 2022; Kameda and Okada, 2023; Reeder et al., 2022), and promoting thermal regulation techniques for human comfort (Ma et al., 2021; Xue et al., 2024). With ongoing technological advancements in thermal systems, with an emphasis on quality of life, and heightened environmental awareness, the focus on cooling strategies has evolved from merely developing high-efficiency thermal control methods to designing lightweight, miniature, and targeted thermal management devices. This interest exists particularly in areas of bio-interfaced microelectronics and medical devices where thermoregulation is a critical physiological process that underpins health and wellness. As new bioelectronic cooling technologies designed for operation outside hospitals and clinics, with capabilities in continuous and on-demand monitoring and thermal regulation, it becomes important to consider the influence of non-expert user placement in the context of tissue mechanics and deformations. Ensuring that physiologically relevant strain levels, which occur during the conformal integration of the device into soft tissues, are accurately captured is crucial since external mechanical fields can deform critical device dimensions and affect the heat transfer efficiency.

In the context of microelectronic devices, the miniaturization of cooling systems holds significant importance. In recent years, cooling modules and interfaces have been combined with conventional electronic systems for thermal control (Dhumal et al., 2023;

Mathew and Krishnan, 2021). In medical applications, cooling technology serves multiple purposes, including pain management and discomfort reduction during treatment and mitigation of adverse effects post-treatment (Cooper et al., 2023; Koç et al., 2006). While extensive cooling can alleviate pain temporarily, it may also adversely affect neighboring tissues as extreme temperatures and temperature gradients can alter biological functions. Localized targeted cooling offers a promising solution for on-demand pain relief (Reeder et al., 2022), inflammation reduction (Fujishima et al., 1995), and bleeding control (Barker et al., 1965). The key lies in controlling the depth, distribution, and extent of cooling to localize the thermal effect to the target areas without affecting surrounding tissue.

Researchers have proposed several approaches and techniques for temperature reduction and management, including air cooling (E et al., 2018), liquid cooling (Bar-Cohen et al., 2006; Gullbrand et al., 2019), thermoelectric cooling (Chen and Liu, 2022; Zaferani et al., 2021), and phase change cooling (Du et al., 2018; Lu, 2000; Tan and Tso, 2004), among others. Notably, the phase change cooling method offers distinct advantages such as rapid heat absorption, significant cooling capacity, low inflow temperature requirements, all without additional energy consumption for heat absorption. These attributes make phase change cooling suitable for implementation in multiple environments, such as biomedical systems and other devices that require thermal management, which has led to a range of applications. Fundamentally, the phase change method relies on rapidly absorbing heat that typically triggers a transition from liquid to vapor phase. Therefore, by leveraging the chemistry and phase change theory of saturated vapor pressure, targeted and adjustable cooling can be attained and implemented in a controlled fluidic system.

Most research on cooling technology focuses on enhancing the cooling efficiency and designing cooling equipment structures. However, as microelectronics and biomedical technologies continue to advance, a growing emphasis is on localized cooling for thermoregulatory control in both microelectronic devices and human tissues. Achieving precise targeted temperature control remains a challenging aspect of current research in biomedical technologies as the fundamental heat transfer mechanisms can vary widely across biological tissues and device layouts. In our previous work (Reeder et al., 2022), we developed a soft bioresorbable cooler, as illustrated in Fig. 1, that uses the phase-change in microfluidic channels to achieve precise targeted cooling for nerve conduction blockage. The result provides on-demand pain relief as an alternative to highly addictive opioids for treating pain. This system exhibits excellent thermal management and cooling capabilities for localized thermal blocking. In this study, we introduced nitrogen and perfluoropentane (PFP) liquid into the microchannels for mixing. The interaction between the two leads to vaporization of the PFP liquid, which absorbs heat. Simultaneously, nitrogen gas is introduced in the microfluidic system to carry the low-temperature gas resulting from the reaction further into the microfluidic channel. As a result, this low-temperature gas exchanges heat with the surrounding tissue, effectively reducing its temperature and producing the nerve-blocking effect.

In this paper, we propose a theoretical model, building upon our previous work (Reeder et al., 2022), to simulate the cooling process of the fluid by the gas mixture occurring in the deformable microfluidic channels. We also describe the heat transfer mechanisms that govern the cooling process for physiologically relevant parameters. In addition, we consider the flow rate of the fluid inside the microfluidic channel and the effect of changes in channel dimensions due to tissue deformation on heat transfer mechanisms. Finite element analysis (FEA) is used to numerically determine the temperature distribution in the fluid and the surrounding tissue for the set of experimental variables used in our previous nerve-blocking application. Subsequently, we establish a scaling law to describe the cooling effect of the microfluidic structure on the tissue through a set of non-dimensional parameters that can be used to locally control the cooling process. Lastly, we determine the optimal ratio and quantity of the two gases required to flow into the microfluidic cooler, based on the desired temperature reduction goals and the results of the scaling law, to provide guidance for the practical operation of the device.

The article is organized as follows: First, in Section 2, we establish the model for the vaporization of the liquids to identify the key

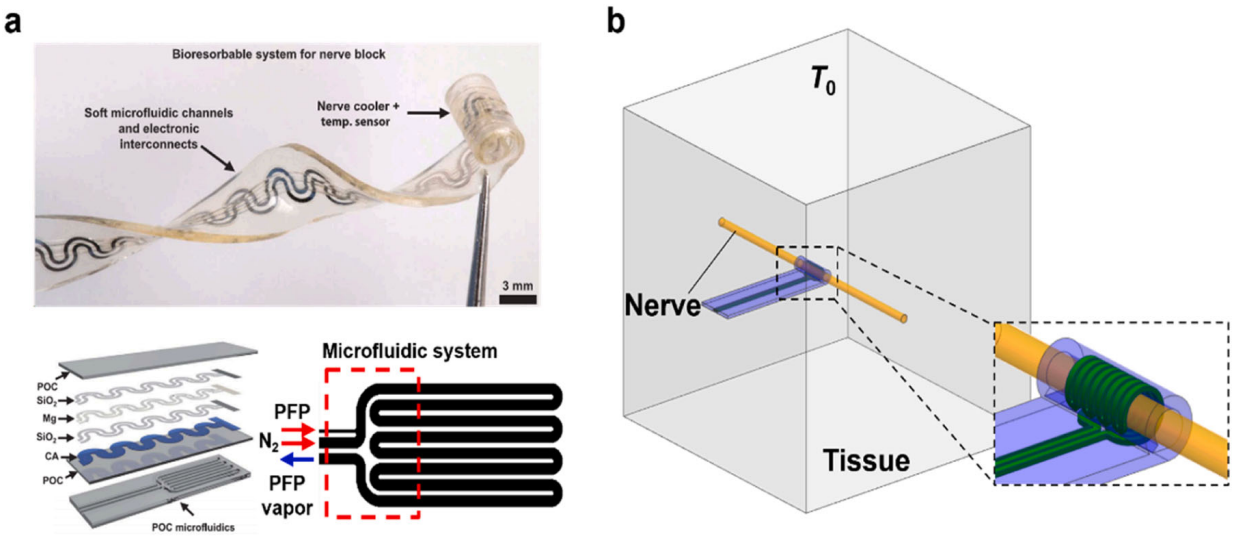

Fig. 1. (a) Diagram of the soft, bioresorbable, evaporative microfluidic cooler for an on-demand nerve block application; Reprinted with permission from (Reeder et al., 2022)Copyright 2022, AAAS. (b) 3D model of the nerve, wrapped by the microfluidic cooler, embedded in the tissue.

parameters governing the phase change and define the variables controlling the target cooling. Then, in Section 3, a mechanical analysis is presented to describe the influence of applied strain in the tissue on the deformation of microfluidic channels. A thermal analysis is presented to discuss the effect of fluid viscosity. The steady-state temperature distributions are solved from the heat transfer equation. A scaling law is built to quantify the spatial temperature distribution of tissue considering the deformation of microfluidic channels. In Section 4, we examine the effects of the fluid, heat transfer coefficient, validating the assumptions to simplify the scaling analysis to capture only cooling effects due to heat convection in the microchannels and surrounding tissue. Finally, Section 5 discusses the framework for determining the required amounts of gas and liquid inside the microchannels to locally achieve a desired temperature change.

2. Model of the vaporization of liquids

The microfluidic cooler is supplied with liquid A and gas B concurrently. The vaporization reaction between liquid A and gas B in the microfluidic channel can be represented by the following equation

$$\xi A_{liquid} + B_{gas} \rightarrow \xi A_{gas} + B_{gas} \tag{1}$$

where ξ is the molar ratio of liquid A to gas B (ξ mol of liquid A for 1 mol of gas B in the above reaction); for each liquid, ξ depends on temperature T as given by $\xi = \frac{P(T)}{P_0}$. Here P_0 is the standard atmospheric pressure, and $P(T)$ is the saturated vapor pressure, i.e., the maximum pressure achieved by the volatilization of a liquid in a confined space and it depends on the temperature T. This saturated vapor pressure $P(T)$ is measured experimentally and is considered known for each liquid (Crowder et al., 1967), therefore so is ξ as a function of temperature. Let ΔH denote the enthalpy change of liquid A during evaporation, which is considered a known property of each liquid (Cachadiña and Mulero, 2009). The heat absorbed for complete vaporization is then given by $\xi \Delta H$.

Let X denote the quantity (mol) of gas B passing through per unit time. The quantity of gas A (after liquid evaporation) is then ξX. The volume (per unit time) of the mixed gases is $X(1+\xi)V_m$, where $V_m = 0.00224\ \mathrm{m}^3/\mathrm{mol}$ is the molar volume of gas, which gives the average flow rate v in the cross section in Eq. (2). For ξX mol of liquid A (per unit time), the heat absorption Q per unit time due to evaporation of liquid A is, therefore, $\xi X \Delta H$, i.e.,

$$\begin{cases} v = \dfrac{4X(1+\xi)V_m}{\pi d^2} \\ Q = \xi X \Delta H \end{cases} \tag{2}$$

where d is the diameter of the microfluidic channel.

In the mixture of gases A and B, the volume fraction β and mass fraction γ of A are given by

$$\beta = \frac{M_A \rho_A}{M_A \rho_A + (1/\xi) M_B \rho_B} \tag{3}$$

$$\gamma = \frac{M_A}{M_A + (1/\xi) M_B} \tag{4}$$

where M_A and M_B are the molar mass of gas A and gas B, respectively. The effective specific heat capacity c_f, density ρ_f, and thermal conductivity λ_f of the fluid (mixture of gases A and B) is given by

$$c_f = \frac{\xi}{1+\xi} c_A + \frac{1}{1+\xi} c_B \tag{5}$$

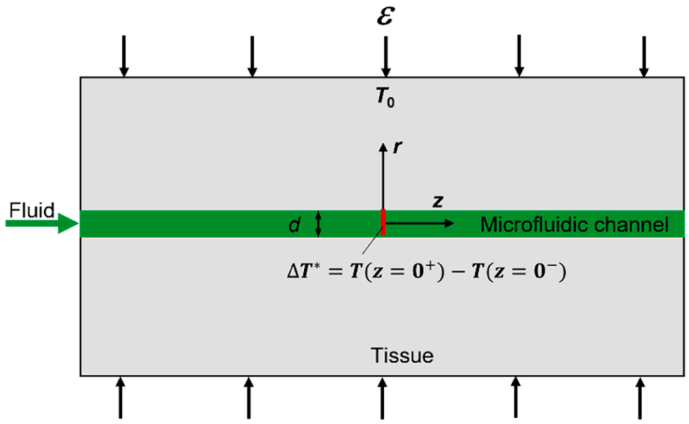

Fig. 2. Theoretical model of the microfluidic cooler inside the tissue.

$$\rho_f = \beta\rho_A + (1-\beta)\rho_B \tag{6}$$

$$\lambda_f = \gamma\lambda_A + (1-\gamma)\lambda_B \tag{7}$$

where c_A and c_B are specific heat capacity, ρ_A and ρ_B are density, λ_A and λ_B are the thermal conductivity of gas A and gas B, respectively.

3. Mechanics and thermal analysis

A three-dimensional model in cylindrical coordinate for the cooling mechanism of the tissue by a microfluidic nerve-cooler is established in this section. Fig. 2 shows an infinite tissue, containing a microfluidic channel (along z axis) with diameter d of the circular cross section. Tissue cooling is regulated primarily by the flow rate. On the left side of the channel ($z < 0$), a mixed fluid flows at an average flow rate v, undergoes the reaction in Eq. (1) at the section $z = 0$ (indicated by the solid red line in Fig. 2), then continues to flow to the right side of the channel ($z > 0$) at the same average flow rate. The local cooling of the tissue using a microfluidic nerve-cooler, resulting in the vaporization of the liquid and heat absorption, is modelled by

$$Q = \frac{\pi}{4} c_f \rho_f v d^2 \Delta T^* \tag{8}$$

where $\Delta T^* = T(z=0^+) - T(z=0^-)$ is the temperature jump at the section $z = 0$ due to reaction; $\pi v d^2/4$ represents the volume flow rate such that $\pi\rho_f v d^2/4$ is the mass flow rate, and its product with c_f and ΔT^* gives the heat absorption per unit time. FEA is adopted to determine the temperature distribution in the fluid and the surrounding tissue (details in Appendix A).

The temperature change ΔT (from the environment temperature T_0) of tissue is influenced by three sets of variables and parameters: 1) the position (r, z); 2) the diameter d of microfluidic channel, and material properties such as the viscosity μ_f, density ρ_f, heat capacity c_f and the thermal conductivity λ_f of the fluid as well as the density ρ_t, the heat capacity c_t, the thermal conductivity λ_t, the elastic modulus E and the Poisson's ratio υ of the tissue; and 3) the applied strain ε in the tissue, the flow rate v of the fluid, and the heat absorption Q per unit time. This relation can be symbolically expressed as

$$\Delta T = \Delta T\left(r, z, d, c_f, \rho_f, \lambda_f, c_t, \rho_t, \lambda_t, \mu_f, E, \upsilon, v, \varepsilon, Q\right) \tag{9}$$

The baseline values for these properties are $d = 0.25$ mm, c_f=947.3 J/(kg ·K), $\rho_f = 4.465$ kg/m^3, $\lambda_f = 0.0782$ W/(m·K), c_t=4120 J/(kg ·K), $\rho_t = 998$ kg/m^3, $\lambda_t = 0.625$ W/(m·K) and $\mu_f = 1.7 \times 10^{-5}$ kg/m·s (Reeder et al., 2022). The initial temperature is 37 °C for both the tissue and inlet fluid.

First, we discuss the applied (compressive) strain ε along the radial direction r in the tissue, originating from the user during placement to attach the bioelectronic into the tissue. The microfluidic channel deforms accordingly; along its length direction it extends by $1 + 2\upsilon\varepsilon$ due to Poisson's effect in the tissue; and its diameter changes from d to d'. The ratio of the channel volumes after and before the deformation

$$\frac{Vol}{Vol_0} = \frac{d'^2(1+2\upsilon\varepsilon)}{d^2} \tag{10}$$

The initial pressure p_0 in the microfluidic channel changes to $p = p_0 + \Delta p$ after deformation. The ideal gas law gives

$$\frac{\pi}{4} d^2 p_0 = \frac{\pi}{4} d'^2 (p_0 + \Delta p)(1 + 2\upsilon\varepsilon) \tag{11}$$

For an infinite solid containing a cylindrical hole subject to remote compressive strain ε along the radial direction and internal pressure Δp inside the hole, its diameter change is given by (Sitharam and Govindaraju, 2021)

$$d - d' = \frac{2\varepsilon d}{1-\upsilon} - \frac{(1+\upsilon)\Delta p d}{E} \tag{12}$$

Elimination of Δp from Eqs. (11) and (12) yields the governing equation for d' as

$$A\left(\frac{d}{d'}\right)^3 + B\left(\frac{d}{d'}\right) - 1 = 0 \tag{13}$$

$$\begin{cases} A = \dfrac{p_0(1+\upsilon)}{E(1+2\upsilon\varepsilon)} \\ B = \dfrac{E(1-\upsilon) - 2E\varepsilon - (1-\upsilon^2)p_0}{E(1-\upsilon)} \end{cases} \tag{14}$$

Its solution is

$$d' = d\left\{\left(\frac{1}{2A}+\sqrt{\frac{B^3}{27A^3}+\frac{1}{4A^2}}\right)^{1/3}+\left(\frac{1}{2A}-\sqrt{\frac{B^3}{27A^3}+\frac{1}{4A^2}}\right)^{1/3}\right\}^{-1} \tag{15}$$

The temperature change in Eq. (9) can be simplified as

$$\Delta T = \Delta T\left(r, z, d', c_f, \rho_f, \lambda_f, c_t, \rho_t, \lambda_t, \mu_f, v, Q\right) \tag{16}$$

The range of viscosity for common gas is from 0.8×10^{-5} kg/(m·s) to 2×10^{-4} kg/(m·s) (Lemmon and Jacobsen, 2004). For these two limits, Fig. 3 shows the distributions of temperature change ΔT over the space $-40d' < z < 40d'$, $0 < r < 40d'$ at a representative average flow rate $v = 35$ m/s. It clearly indicates that the temperature distribution is essentially independent of the viscosity.

Fig. 4 shows the temperature change at a fixed point versus the viscosity μ_f at different flow rates v. It confirms that the viscosity has little effect on the temperature distribution. Therefore the temperature change in Eq. (16) can be further simplified as

$$\Delta T = \Delta T(r, z, d', c_f, \rho_f, \lambda_f, c_t, \rho_t, \lambda_t, v, Q) \tag{17}$$

In the following we neglect the effect of fluid viscosity such that the flow rate is uniform in the microfluidic channel. The steady-state temperature distribution T is governed by the heat transfer equation (Webb et al., 2015; Frantz et al., 2023)

$$\frac{1}{r}\frac{\partial}{\partial r}\left(\lambda_f r\frac{\partial T}{\partial r}\right)+\frac{\partial}{\partial z}\left(\lambda_f\frac{\partial T}{\partial z}\right)=\rho_f c_f v\frac{\partial T}{\partial r} \tag{18}$$

The steady heat transfer equation in the tissue is (Webb et al., 2015)

$$\frac{1}{r}\frac{\partial}{\partial r}\left(\lambda_t r\frac{\partial T}{\partial r}\right)+\frac{\partial}{\partial z}\left(\lambda_t\frac{\partial T}{\partial z}\right)=0 \tag{19}$$

The environmental temperature T_0 is imposed as the remote boundary condition for the tissue. The interface between the fluid and the tissue satisfies the continuity conditions

$$[T] = 0 \tag{20}$$

$$[\lambda \partial T/\partial n] = 0 \tag{21}$$

where [..] stands for the jump across the interface, and n is the normal of the interface.

Based on the equations presented in this section, the difference between the steady-state temperature field inside the tissue and the environment temperature $\Delta T = T\text{-}T_0$ is linearly proportional to the heat absorption per unit time Q. Its spatial distribution depends primarily on the flow rate v, which always scales with $\rho_f c_f$ as in Eq. (18). Other properties that come into analysis include the thermal conductivity λ_f for the fluid and λ_t for the tissue; and the microfluidic channel size d'. The normalized, dimensionless temperature difference $\Delta T\lambda_t d'/Q$ depends on the normalized position (r/d', z/d'), normalized flow rate $vc_f\rho_f d'/\lambda_t$, the conductivity ratio λ_f/λ_t, which yields a scaling law for the temperature distribution

$$\frac{\Delta T d'\lambda_t}{Q} = f\left(\frac{r}{d'}, \frac{z}{d'}, \frac{vc_f\rho_f d'}{\lambda_t}, \frac{\lambda_f}{\lambda_t}\right) \tag{22}$$

4. Numerical results and a simplified scaling law

For representative tissue and gases used in microfluidic nerve-cooler system, their thermal conductivity ratio λ_f/λ_t always ranges between 0.1 and 0.3 (Reeder et al., 2022). Fig. 5 shows the normalized temperature distribution $\Delta T\lambda_t d'/Q$ for two limits, λ_f/λ_t =0.1 and 0.3 over the space $-40 < z/d' < 40$, $0 < r/d' < 40$, when the normalized flow rate is $vc_f\rho_f d'/\lambda_t$ =30.

The nearly identical distributions in Fig. 5 for λ_f/λ_t =0.1 and 0.3 suggest that, for $vc_f\rho_f d'/\lambda_t$ =30, the changes in tissue or fluid

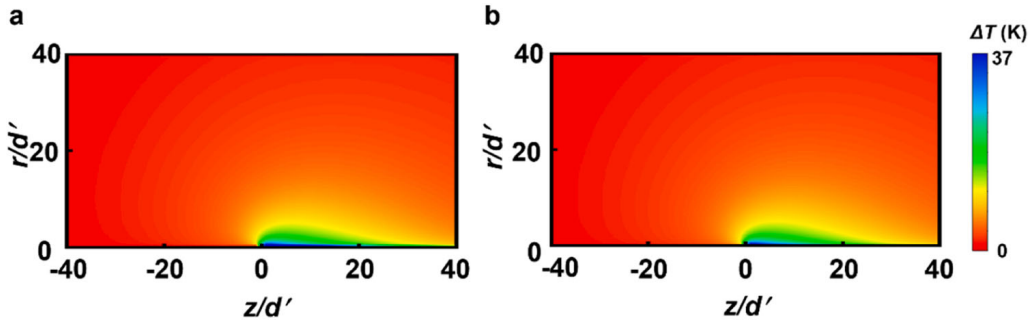

Fig. 3. The distribution of the temperature change (ΔT) with (a) $\mu_f = 0.8 \times 10^{-5}$ (kg/m·s), and (b) $\mu_f = 2 \times 10^{-4}$ (kg/m·s) at $v = 35$ m/s.

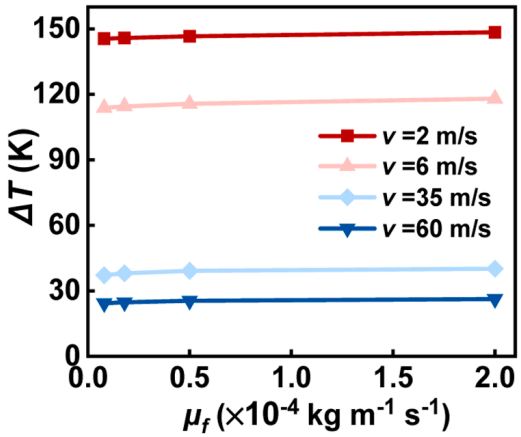

Fig. 4. The temperature change (ΔT) at point $z = d'$, $r = 0.5d'$ versus μ_f for several flow rate v.

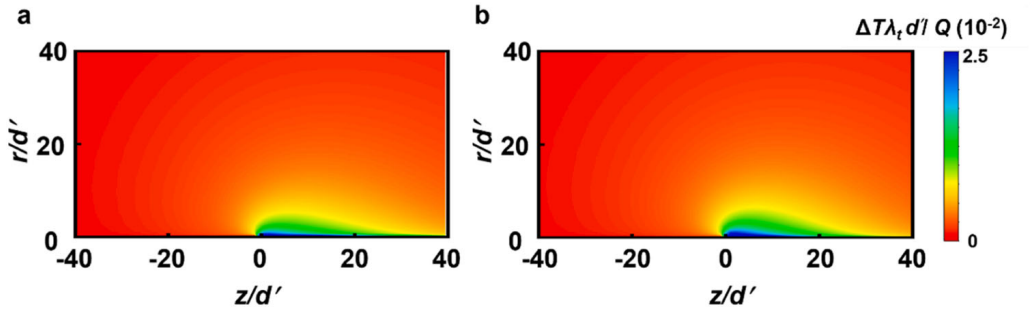

Fig. 5. The distribution of the normalized temperature change ($\Delta Td'\lambda_t/Q$) with (a) λ_f/λ_t=0.1, and (b) λ_f/λ_t=0.3 at $vc_f\rho_f d'/\lambda_t$ =30.

conductivity have minimal impact on the scaling law results. In other words, for the current set of fluid rate and thermal properties in the working process of microfluidic nerve-cooler system, the non-dimensional temperature distribution is approximately independent of the value of λ_f/λ_t.

Fig. 6 shows the normalized temperature change at a fixed point (r/d', z/d')=(1,1/2) versus the thermal conductivity ratio λ_f/λ_t for a wide range of flow rate $vc_f\rho_f d'/\lambda_t$. It confirms the conclusion from Fig. 5 that, at a relatively large flow rate, the normalized temperature change is independent of the conductivity ratio λ_f/λ_t. However, at a low flow rate such as $vc_f\rho_f d'/\lambda_t$=2, the value of λ_f/λ_t has a slight effect on the temperature change $\Delta Td'\lambda_t/Q$ (Fig. 6). This is due to the influence of convective and conductive heat transfer in the working process of microfluidic nerve-cooler system. At high flow rates, the dominant cooling mechanism of microfluidic nerve-cooler system is convection due to the fluid flow. At low flow rates, e.g., $vc_f\rho_f d'/\lambda_t < 5$, the effect of the thermal conductivity in the tissue and channel cannot be neglected since there is a combined convection-conduction effect to produce a different thermal response. However, for practical implementation of the microfluidic cooling system, the dimensionless flow rate will always satisfy $vc_f\rho_f d'/\lambda_t > 30$ and the

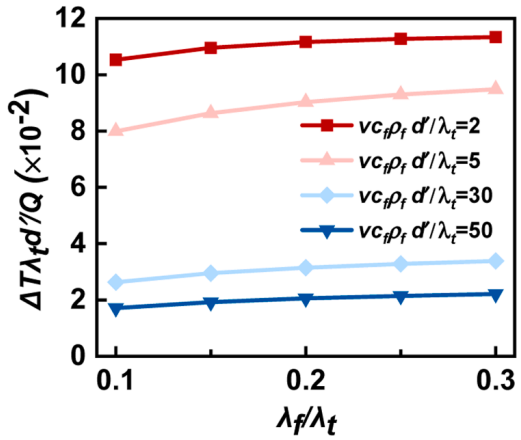

Fig. 6. The normalized temperature change ($\Delta Td'\lambda_t/Q$) at point z/d'=1, r/d'=1/2 versus λ_f/λ_t for several normalized flow rate $vc_f\rho_f d'/\lambda_t$.

dimensionless group λ_f/λ_t can be omitted from the scaling law, i.e.,

$$\frac{\Delta T d'\lambda_t}{Q} = f\left(\frac{r}{d'}, \frac{z}{d'}, \frac{vc_f\rho_f d'}{\lambda_t}\right) \tag{23}$$

which depends on the normalized average flow rate in addition to the position.

5. Required amount of fluids for targeted local cooling

The microfluidic nerve-cooler system (Reeder et al., 2022) operates on internal fluid flow rate control, resulting in varying degrees of temperature reduction in tissue for different nitrogen (gas B) and PFP (liquid A) flow rates. The scaling law established in the present study indicates that the distribution of the normalized temperature change $\Delta Td'\lambda_t/Q$ within the tissue is primarily governed by the normalized flow rate $vc_f\rho_f d'/\lambda_t$. In experiments, however, it is an inverse problem – What are the amounts of gas B and liquid A (i.e., X and ξX in Section 2) in experiments for a given targeted cooling temperature at the nerve? In the following, we demonstrate an example to straightforwardly determine these important input variables in experiments.

We use the average temperature change $\Delta T^*=\Delta T(z=0^+)$ (at the section at $z=0^+$, immediately to the right of the section where the reaction occurs) as an example, and the temperature change is averaged over the cross section of the microfluidic channel. Fig. 5(a) shows this normalized average temperature change decreases monotonically as the normalized flow rate $vc_f\rho_f d'/\lambda_t$ increases, asymptotically approaching zero. For a targeted cooling ΔT^*, Fig. 5(a) does not immediately yield the values of X for gas B and ξX for liquid A needed in experiments.

After substituting the expressions v and Q in terms of X in Eq. (2), the normalized temperature change and normalized velocity become

$$\frac{\Delta T d'\lambda_t}{Q} = \frac{\Delta T d'\lambda_t}{X\xi\Delta H} \tag{24}$$

$$\frac{vc_f\rho_f d'}{\lambda_t} = \frac{4X(1+\xi)V_m c_f\rho_f}{\pi d'\lambda_t} \tag{25}$$

Multiplying Eq. (24) with Eq. (25) gives

$$\frac{\Delta T d'\lambda_t}{Q}\cdot\frac{vc_f\rho_f d'}{\lambda_t} = \frac{1+\xi}{\xi}\cdot\frac{4\Delta T V_m c_f\rho_f}{\pi\Delta H} \tag{26}$$

which is independent of X and d'. Fig. 7(b) shows this product in Eq. (26) [multiplication of Eqs. (24) and (25)] versus the new normalization of flow rate in Eq. (25).

For a representative elastic modulus of tissue E = 25 kPa (Chen et al., 2024), Poisson's ratio 0.48 for a nearly incompressible material, and initial pressure p_0=100 kPa (Reeder et al., 2022). Fig. 8 shows the product in Eq. (26) versus the normalized flow rate using the initial diameter d of the microfluidic channel instead d', i.e., $4X(1+\xi)V_m c_f\rho_f/(\pi d\lambda_t)$ [which comes from Eq. (25) by replacing d' with d, which are related via Eq. (15)]. For the applied compressive strain in tissue ε=0, 10 % and 20 %, the curves in Fig. 8 all coincide, which suggests independence of the tissue strain, i.e., the tissue deformation has a very minor effect on the determination of the X based on Fig. 8.

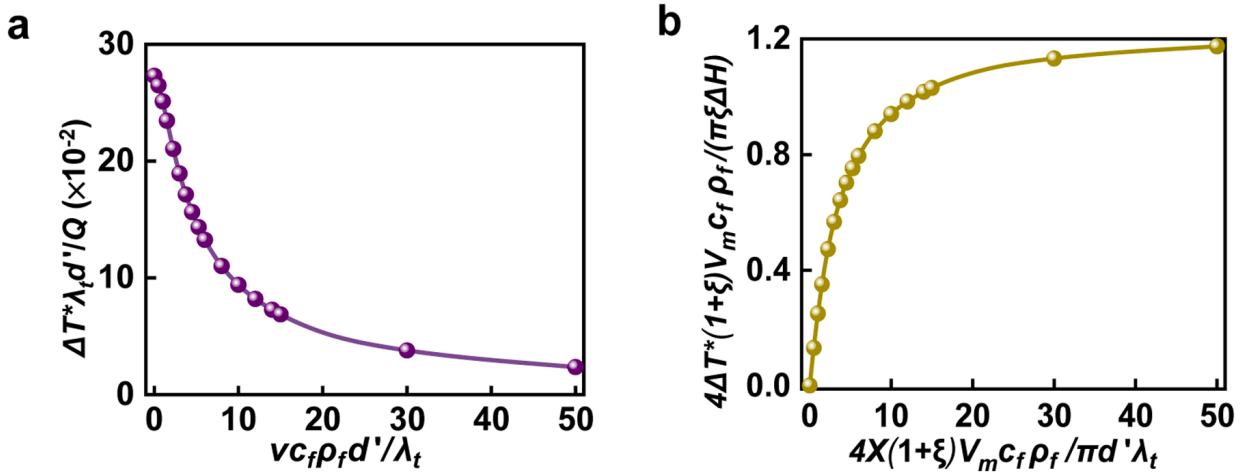

Fig. 7. (a) The normalized average temperature change $\Delta T^* d'\lambda_t/Q$ versus the normalized flow rate $vc_f\rho_f d'/\lambda_t$, where ΔT^* is the average over the cross-section of reaction ($z=0^+$, immediately to the right of the section $z=0$ where the reaction occurs) in the microfluidic channel; (b) Replot of the curve in (a) to determine the amount of input fluids (gas B and liquid A).

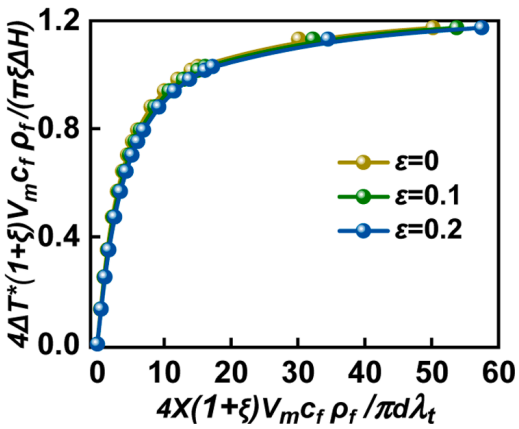

Fig. 8. Replot of the curve in Fig. 7(b) using the initial diameter d of the microfluidic channel, for the applied compressive strain ε=0, 10 % and 20 % in the tissue.

For a given target temperature change ΔT^* determined from the physiological application, the value of ξ is known from the saturated vapor pressure P by $\xi = P(T_0\text{-}\Delta T^*)/P_0$, where $T_0\text{-}\Delta T^*$ is the local temperature. Therefore, the vertical coordinate in Fig. 8 is known. The curve in Fig. 8 then gives the corresponding horizontal coordinate, which determines the value of X.

Additionally, Fig. 7(b) and Fig. 8 demonstrate that there exists a limit to the cooling capacity of the microfluidic cooler for a given gas, corresponding to the horizontal asymptotes in the figures. Once this cooling limit is reached, further adjusting the fluid flux is no longer an effective strategy for cooling the surrounding tissue. Such an approach to determine the amounts of fluid (X for gas B and ξ^*X for liquid A) for a given targeted temperature change can be straightforwardly extended to any location in the tissue, such as the nerve if its location is known.

6. Conclusion

A theoretical model is proposed to describe and quantify localized tissue cooling using microfluidic nerve-cooler system that rely on fluid phase change to trigger the heat transfer mechanisms in specific tissue locations. The mechanics and thermal analyses account for the effects of tissue deformation and viscous flow in the microfluidic channel on the temperature distribution in the tissue. A scaling law is established to characterize the spatial distribution of steady-state temperature changes within the tissue for a physiologically relevant combination of non-dimensional parameters considering the deformation of microfluidic channel. For the high range of non-dimensional flow rate used to achieve tissue cooling, the influence of the thermal conductivity ratio between the fluid and the tissue was minimal on the dimensionless temperature change. Instead, the key parameters that influence the thermal cooling process are the amounts of liquid and gas, and the expected temperature change determined by the biological application. The proposed scaling law shows that for a given liquid, there is a limit to the targeted temperature change where higher flow rates will not produce further localized temperature reduction. Such an approach is readily applied to nerve cooling.

Statement of novelty

We proposed a theoretical model, based on mechanics and thermal analysis of bioelectronic systems, to evaluate the cooling effect of deformable microfluidic channel coolers driven by liquid phase change heat absorption subjected to an applied strain remotely. The established scaling law model examines the steady-state temperature changes across the tissue for relevant mechanics and thermal parameters. By identifying the governing heat transfer mechanism at high dimensionless flowrates, we illustrate and verify the minimal impact of the ratio of common fluid-tissue thermal conductivities, fluid viscosity, applied remote strain, and present a simplified scaling law model for further thermal analysis. By integrating the theory of phase transitions and saturated vapor pressure, we determine the inlet flow rate of fluid and gas required to achieve specific temperature reduction targets for precise thermal management in bioelectronic systems for physiological applications. Additionally, the scaling law allows for accurate prediction of the theoretical maximum cooling achieved for a given fluid where the mechanics and thermal analysis show the influence of the relevant non-dimensional parameters. This theoretical model can guide the design of liquid phase-change heat-absorbing microfluidic channel coolers for precise cooling and is applicable across a wide range of thermal management scenarios.

CRediT authorship contribution statement

Dongjun Bai: Writing – original draft, Methodology, Investigation, Formal analysis. **Zichen Zhao:** Writing – original draft, Methodology, Investigation, Formal analysis. **Raudel Avila:** Writing – review & editing. **Danli Xia:** Formal analysis. **Yonggang Huang:** Writing – review & editing, Conceptualization. **John A. Rogers:** Writing – review & editing, Conceptualization. **Zhaoqian Xie:** Writing – review & editing, Supervision, Methodology, Investigation, Funding acquisition, Formal analysis, Conceptualization.

Declaration of competing interest

The authors declare that they have no known competing financial interests or personal relationships that could have appeared to influence the work reported in this paper.

Data availability

Data will be made available on request.

Acknowledgments

Zhaoqian Xie acknowledges support from the National Natural Science Foundation of China (12072057), Dalian Outstanding Young Talents in Science and Technology (2021RJ06). Raudel Avila acknowledges support from the ASME Haythornthwaite Foundation Research Initiation Grant.

Appendix A. Finite element analysis (FEA)

The energy and standard k-e models in the commercial FEA software Ansys Fluent were adopted to calculate the temperature change in the fluid and tissue. Hexahedral elements were used for mesh with the minimum element size being one-tenth of the microfluidic channel's radius. Convergence tests of the mesh size were performed to ensure accuracy. A radiator boundary condition was added in the section $z = 0$ of the microfluidic channel with heat flux to simulate the temperature change induced by the vaporization of liquid A (as shown in Fig. 2).

References

Bar-Cohen, A., Arik, M., Ohadi, M., 2006. Direct liquid cooling of high flux micro and nano electronic components. Proceed. IEEE 94 (8), 1549–1570. https://doi.org/10.1109/JPROC.2006.879791.

Barker, C.F., Nance, F.C., Nelson, H.M., Peskin, G.W., Fitts, W.T., 1965. Local hypothermia for the control of bleeding in the large bowel and measurements of inferior mesenteric blood flow during colonic cooling. Am. J. Surg. 109 (1), 84–88. https://doi.org/10.1016/S0002-9610(65)80108-8.

Cachadiña, I., Mulero, A., 2009. New corresponding states model for the estimation of the vaporization enthalpy of fluids. Fluid Phase Equilib. 287 (1), 33–38. https://doi.org/10.1016/j.fluid.2009.09.003.

Chen, Z.-G., Liu, W.-D., 2022. Thermoelectric coolers: infinite potentials for finite localized microchip cooling. J. Mater. Sci. Technol. 121, 256–262. https://doi.org/10.1016/j.jmst.2021.12.069.

Chen, Y., Zhou, Y., Hu, Z., Lu, W., Li, Z., Gao, N., Liu, N., Li, Y., He, J., Gao, Q., Xie, Z., Li, J., He, Y., 2024. Gelatin-based metamaterial hydrogel films with high conformality for ultra-soft tissue monitoring. Nano-Micro Lett 16 (1), 34. https://doi.org/10.1007/s40820-023-01225-z.

Cooper, J., Joseph, C., Kulstad, E., Aslam, K., 2023. Po-02-064 reduced post-ablation chest pain with active esophageal cooling. Heart Rhythm 20 (5), S336. https://doi.org/10.1016/j.hrthm.2023.03.782.

Crowder, G.A., Taylor, Z.L., Reed, T.M., Young, J.A., 1967. Vapor pressures and triple point temperatures for several pure fluorocarbons. J. Chem. Engineer. Data 12 (4), 481–485. https://doi.org/10.1021/je60035a005.

Dhumal, A.R., Kulkarni, A.P., Ambhore, N.H., 2023. A comprehensive review on thermal management of electronic devices. J. Engineer. Appl. Sci. 70 (1), 140. https://doi.org/10.1186/s44147-023-00309-2.

Do, N.B.D., Andreassen, E., Edwardsen, S., Lifjeld, A., Aasmundtveit, K.E., Nguyen, H.-V., Imenes, K., 2022. Thermal management of an interventional medical device with double layer encapsulation. Experiment. Heat Transf. 35 (5), 708–725. https://doi.org/10.1080/08916152.2021.1946208.

Du, K., Calautit, J., Wang, Z., Wu, Y., Liu, H., 2018. A review of the applications of phase change materials in cooling, heating and power generation in different temperature ranges. Appl. Ener. 220, 242–273. https://doi.org/10.1016/j.apenergy.2018.03.005.

E, J., Yue, M., Chen, J., Zhu, H., Deng, Y., Zhu, Y., Zhang, F., Wen, M., Zhang, B., Kang, S, 2018. Effects of the different air cooling strategies on cooling performance of a lithium-ion battery module with baffle. Appl. Therm. Eng. 144, 231–241. https://doi.org/10.1016/j.applthermaleng.2018.08.064.

Frantz, R.A.S., Loiseau, J.-Ch., Robinet, J.-Ch., 2023. Krylov methods for large-scale dynamical systems: application in fluid dynamics. Appl. Mech. Rev. 75 (3) https://doi.org/10.1115/1.4056808.

Fujishima, H., Yagi, Y., Toda, I., Shimazakl, J., Tsubota, K., 1995. Increased comfort and decreased inflammation of the eye by cooling after cataract surgery. Am. J. Ophthalmol. 119 (3), 301–306. https://doi.org/10.1016/S0002-9394(14)71171-7.

Ghasemi Zavaragh, H., Kaleli, A., Afshari, F., Amini, A., 2017. Optimization of heat transfer and efficiency of engine via air bubble injection inside engine cooling system. Appl. Therm. Eng. 123, 390–402. https://doi.org/10.1016/j.applthermaleng.2017.04.164.

Gullbrand, J., Luckeroth, M.J., Sprenger, M.E., Winkel, C., 2019. Liquid cooling of compute system. J. Electr. Packag. 141 (1), 010802 https://doi.org/10.1115/1.4042802.

Habibi Khalaj, A., Halgamuge, S.K., 2017. A Review on efficient thermal management of air- and liquid-cooled data centers: from chip to the cooling system. Appl. Ener. 205, 1165–1188. https://doi.org/10.1016/j.apenergy.2017.08.037.

Kameda, N., Okada, S., 2023. Evaluation of postoperative warming care protocol for thermal comfort and temperature management immediately after surgery: nonrandomized controlled trial. J. PeriAnesthesia Nurs. 38 (3), 427–433. https://doi.org/10.1016/j.jopan.2022.07.001.

Koç, M., Tez, M., Yoldaş, Ö., Dizen, H., Göçmen, E., 2006. Cooling for the reduction of postoperative pain: prospective randomized study. Hernia 10 (2), 184–186. https://doi.org/10.1007/s10029-005-0062-2.

Kong, G., Xu, J., Xie, W., Sun, Y., Fan, Y., Wang, H., Kondo, H., Zhou, H., 2023. Dual-mode smart flipping materials and devices for thermal management. Interdisciplin. Mater. 2 (5), 735–760. https://doi.org/10.1002/idm2.12123.

Lemmon, E.W., Jacobsen, R.T., 2004. Viscosity and thermal conductivity equations for Nitrogen, Oxygen, Argon, and Air. Int. J. Thermophys 25 (1), 21–69.

Li, Y.-Z., Wang, Y.-Y., Lee, K.-M., 2010. Dynamic modeling and transient performance analysis of a LHP-MEMS thermal management system for spacecraft electronics. IEEE Transact. Compon. Packag. Technol. 33 (3), 597–606. https://doi.org/10.1109/TCAPT.2010.2049358.

Lu, T.J., 2000. Thermal management of high power electronics with phase change cooling. Int. J. Heat Mass Transf. 43 (13), 2245–2256. https://doi.org/10.1016/S0017-9310(99)00318-X.

Ma, Z., Zhao, D., She, C., Yang, Y., Yang, R., 2021. Personal thermal management techniques for thermal comfort and building energy saving. Mater. Tod. Phy. 20, 100465 https://doi.org/10.1016/j.mtphys.2021.100465.

Mathew, J., Krishnan, S., 2021. A review on transient thermal management of electronic devices. J. Electr. Packag 144 (1), 010801. https://doi.org/10.1115/1.4050002.

Rao, Z., Lyu, P., Du, P., He, D., Huo, Y., Liu, C., 2022. Thermal safety and thermal management of batteries. Battery Ener. 1, 20210019 https://doi.org/10.1002/bte2.20210019.

Reeder, J.T., Xie, Z., Yang, Q., Seo, M.-H., Yan, Y., Deng, Y., Jinkins, K.R., Krishnan, S.R., Liu, C., McKay, S., Patnaude, E., Johnson, A., Zhao, Z., Kim, M.J., Xu, Y., Huang, I., Avila, R., Felicelli, C., Ray, E., Guo, X., Ray, W.Z., Huang, Y., MacEwan, M.R., Rogers, J.A., 2022. Soft, bioresorbable coolers for reversible conduction block of peripheral nerves. Science 377 (6601), 109–115. https://doi.org/10.1126/science.abl8532.

Sitharam, T.G., Govindaraju, L., 2021. Theory of Elasticity. Springer, Singapore. https://doi.org/10.1007/978-981-33-4650-5.

Tan, F.L., Tso, C.P., 2004. Cooling of mobile electronic devices using phase change materials. Appl. Therm. Eng 24 (2–3), 159–169. https://doi.org/10.1016/j.applthermaleng.2003.09.005.

Webb, R.C., Ma, Y., Krishnan, S., Li, Y., Yoon, S., Guo, X., Feng, X., Shi, Y., Seidel, M., Cho, N.H., Kurniawan, J., Ahad, J., Sheth, N., Kim, J., Taylor VI, J.G., Darlington, T., Chang, K., Huang, W., Ayers, J., Gruebele, A., Pielak, R.M., Slepian, M.J., Huang, Y., Gorbach, A.M., Rogers, J.A., 2015. Epidermal devices for noninvasive, precise, and continuous mapping of macrovascular and microvascular blood flow. Sci. Adv 1 (9), e1500701. https://doi.org/10.1126/sciadv.1500701.

Weng, J., Huang, Q., Li, X., Zhang, G., Ouyang, D., Chen, M., Yuen, A.C.Y., Li, A., Lee, E.W.M., Yang, W., Wang, J., Yang, X., 2022. Safety issue on PCM-based battery thermal management: material thermal stability and system hazard mitigation. Ener. Stor. Mater. 53, 580–612. https://doi.org/10.1016/j.ensm.2022.09.007.

Xue, S., Huang, G., Chen, Q., Wang, X., Fan, J., Shou, D., 2024. Personal thermal management by radiative cooling and heating. Nano-Micro Lett 16 (1), 153. https://doi.org/10.1007/s40820-024-01360-1.

Zaferani, S.H., Sams, M.W., Ghomashchi, R., Chen, Z.-G., 2021. Thermoelectric coolers as thermal management systems for medical applications: design, optimization, and advancement. Nano Ener. 90, 106572 https://doi.org/10.1016/j.nanoen.2021.106572.

Zhai, H., Fan, D., Li, Q., 2022. Dynamic radiation regulations for thermal comfort. Nano Ener. 100, 107435 https://doi.org/10.1016/j.nanoen.2022.107435.

Zhang, X., Wang, Z., Huang, G., Chao, X., Ye, L., Fan, J., Shou, D., 2024. Soft robotic textiles for adaptive personal thermal management. Adv. Sci., 2309605 https://doi.org/10.1002/advs.202309605.